Biosensors and Bioelectronics 143 (2019) 111627

Contents lists available at ScienceDirect

Biosensors and Bioelectronics

journal homepage: www.elsevier.com/locate/bios

In situ H_2O_2 generation with gold nanoflowers as the coreactant accelerator for enzyme-free electrochemiluminescent immunosensing

Qiuyu Hu[a], Jianying Yang[b], Zengyao Zheng[b], Yupei Ding[a], Yaowen Chen[c], Wenhua Gao[a,c,*]

[a] Department of Chemistry and Laboratory for Preparation and Application of Ordered Structural Materials of Guangdong Province, Shantou University, Shantou, Guangdong, 515063, PR China

[b] National Detergents and Cosmetics Products Quality Supervision and Inspection Center (Guangdong), Shantou, Guangdong, 515041, PR China

[c] Analysis & Testing Center, Shantou University, Shantou, Guangdong, 515063, PR China

ARTICLE INFO

Keywords:
Electrochemiluminescence
Gold nanoflowers
Hydrogen peroxide
Luminol
AFP
POCTs

ABSTRACT

In traditional electrochemiluminescence (ECL) analysis, gold nanomaterials are commonly used as a tool for signal amplification and linking antibodies due to their good electrical conductivity and biocompatibility. Here, we found that multitipped gold nanoparticles—gold nanoflowers (AuNFs) as coreactant accelerator have good catalytic activity for the reduction of dissolved oxygen (O_2) to hydrogen peroxide (H_2O_2) using tris (hydroxymethyl) aminomethane (Tris) as electron donor. Based on this, a new enzyme-free and label-free ECL immunosensor have been constructed for the detection of α-fetoprotein (AFP). In this system, due to the unique geometric and spatial effects of AuNFs, the dissolved O_2 as endogenous coreactant was catalyzed by AuNFs to produce H_2O_2 using Tris as an electron donor. The in situ generated H_2O_2 can more efficiently produce various electrogenerated reactive oxygen species (ROSs) as the important intermediates on the electrode surface. Then, oxidation of luminol reacts with ROSs significantly amplifies the luminol ECL signal. Under optimal experimental conditions, the proposed ECL immunosensor was able to detect the AFP concentration from 0.01 to 100 ng mL^{-1}, with a low detection limit of 3.4 pg mL^{-1} (S/N = 3). In addition, the prepared ITO-based sensor is similar to a micro-test chip and convenient to use, thus making it suitable for clinical use as a disposable device in point-of-care tests (POCTs).

1. Introduction

Recently, Electrochemiluminescence (ECL) has become a powerful tool for analysis of various samples in multiple applications, such as clinic diagnosis (Fang et al., 2019; Mo et al., 2019), food safety (Gao et al., 2018; Wang et al., 2019), and environmental monitoring (Ye et al., 2016), etc., benefited from its inherent features including simplicity, rapidity and high sensitivity (Farka et al., 2017; Liu et al., 2015; Zhuo et al., 2018). Up to now, three major ECL systems, luminol (Liu et al., 2018; Qiao et al., 2018), metal complexes (Wang et al., 2019), and nanomaterials (Fang et al., 2019; Mo et al., 2019), have been widely explored for the analytical application. Luminol is the most popular luminescent reagent in ECL detection because of its non-toxicity, low oxidation potential and strong luminescence (Liu et al., 2018; Zhang et al., 2016). In order to enhance the luminol ECL signal, H_2O_2 is usually used as a coreactant to accelerate the oxidation of luminol by generating various reactive oxygen species (ROSs) such as superoxide ($O_2^{\bullet-}$) and hydroxyl radical ($^{\bullet}OH$). Whereas, in traditional luminol-H_2O_2 ECL system, H_2O_2 suffered from several serious defects such as low stability under room temperature, making it almost impossible to quantify (Huang et al., 2018). On the other hand, the luminol-glucose oxidase (GODx) system can catalyze the in situ generation of H_2O_2 by glucose and oxygen, but the pH of the system is required to be neutral due to the limitation of activity of GODx (Kitte et al., 2017; Xu et al., 2016b). However, luminol has a weaker ECL signal under neutral conditions than alkaline conditions (Li et al., 2008), thus limiting the extensive application of the luminol-GODx system. Compared with H_2O_2, dissolved O_2 as an endogenous coreactant seemed to be an appropriate candidate in biosensors fabrication in terms of the above concerns. Nevertheless, the ECL reaction efficiency of O_2 with luminol was too low to provide a significant signal amplification. Therefore, it is necessary to explore a new enzyme-free luminol-O_2 system, which can both produce H_2O_2 in situ and improve the luminol ECL signal.

* Corresponding author. Department of Chemistry and Laboratory for Preparation and Application of Ordered Structural Materials of Guangdong Province, Shantou University, Shantou, Guangdong, 515063, PR China.
E-mail address: whgao@stu.edu.cn (W. Gao).

https://doi.org/10.1016/j.bios.2019.111627
Received 25 June 2019; Received in revised form 16 August 2019; Accepted 21 August 2019
Available online 23 August 2019

Gold nanomaterials have attracted great interests in bioassays, especially in electrochemiluminescence due to their large surface area, fascinating optical, electronic, catalytic and good biocompatibility (Dong et al., 2007; Higashi et al., 2018; Song et al., 2010). Assemblies of gold nanoparticles are known to produce collective physical properties due to their unique particle size, spacing, and higher-order structure (Bera et al., 2015; Cui et al., 2012; Higashi et al., 2018; Maity et al., 2014; Xu et al., 2016a), especially in the districts of corners, sharp edges, apexes, and tips (Das and Chini, 2012; Das et al., 2012; Hao et al., 2007; Hrelescu et al., 2011; Myroshnychenko et al., 2012). These regions exhibit highly localized and strongly enhanced electromagnetic (EM) fields, known as plasmonic "hot spots" (Alonso-González et al., 2012; Hrelescu et al., 2011), which can remarkably enhance surface-enhanced Raman scattering (SERS) signals (Alonso-González et al., 2012; Chirumamilla et al., 2014). On the other hand, gold nanomaterials can catalyze many organic, electrocatalytic and gas-phase reactions using their active sites on the surface or the Au/support interface (Daniel and Astruc, 2004). For instance, Sunjie Ye and his colleagues found that gold nanoflowers (AuNFs) have stronger catalytic activity than gold nanoparticles (AuNPs) in the catalytic reduction of *p*-nitrophenol to *p*-aminophenol (Ye et al., 2016). In addition, oxygen adsorbed on the surface of the AuNPs can be catalyzed to produce highly reactive superoxo- or peroxo-like species using poly (N-vinyl-2-pyrrolidone) (PVP) donated electrons (Tsunoyama et al., 2009). Recently, Higashi and co-workers observed that in tris (hydroxymethyl) aminomethane (Tris) solution, AuNPs at about 15 nm can catalyze the reduction of oxygen to ROS. They proposed that aggregation of the AuNPs, in some manner, played a role in enhancing their catalytic activity due to several factors such as spatial effects and the presence of active sites at low-coordination Au atoms and Au/support junctions (Higashi et al., 2018). Therefore, the aggregate state of gold nanoparticles, multitipped structure AuNFs, are responsible for great enhancements in catalytic and optical properties in luminol-O_2 system due to its unique spatial structure. In addition, AuNFs/ITO-based sensors are expected to simplify the inspection process and significantly improve detection performance.

Herein, a novel ECL immunosensor that combines the enzyme-free and label-free strategies and utilizes the catalysis effect of the coreactant accelerator AuNFs was developed. First, we prepared AuNFs with the outer layer covered with a large number of irregularly shaped AuNPs. Subsequently, the AuNFs were assembled on indium tin oxide (ITO) electrode surface via the adhesion of (3-aminopropyl) triethoxysilane (APTES). After being immersed in Tris solution (electron donor) for a while, the high catalytic activity, large surface area, high conductivity, and excellent biocompatibility of AuNFs are used as coreactant accelerator to catalyze the dissolved O_2 to produce H_2O_2 in situ. The generated H_2O_2 can further produce various electrogenerated ROSs on the AuNFs/ITO electrode surface, which accelerate the ECL reaction and enhance the ECL intensity in luminol-O_2 system. After AFP specifically binds to anti-AFP on the final sensor, the ECL signal decreased with increasing AFP concentration due to the specific immunoreaction of the antigen-antibody to block the electron transfer of the ECL reaction (Scheme 1). Moreover, the ECL mechanism of the luminol-O_2 System using AuNFs as the coreactant accelerator was explored.

2. Experimental section

Chemicals and reagents, and apparatus have been reported on Supporting information.

2.1. Synthesis of gold nanoflowers (AuNFs)

AuNFs were prepared in aqueous solutions according to a previous report with some modifications (Li et al., 2017). Briefly, 20 mL of a 0.25 mM $HAuCl_4$ aqueous solution was first heated to boiling and 200 μL of a 5% sodium citrate was added with stirring. The reaction was allowed to run until the color turned into wine red to obtain Au seeds. To grow AuNFs, 50 mL of 0.25 mM $HAuCl_4$ aqueous solution was adjusted to pH 11.5 by 1.0 M NaOH solution. Under mild shaking, the mixture of 4 mL Au seeds and 400 μL $NH_2OH{\cdot}HCl$ solution (40 mM) was added into the above solution at 30 °C. Subsequently, the color of the solution turned from wine red to blue green to obtain AuNFs. The AuNFs solution was centrifuged and thoroughly washed three times with ultrapure water. Thereafter, the obtained AuNFs precipitates were ultrasonically distributed in 5 mL ultrapure water for further experiment.

2.2. Preparation of gold nanoparticles (AuNPs)

To compare the catalytic activities of AuNFs and AuNPs, AuNPs with average size of 15 nm were prepared by the previously reported method (Peng et al., 2007). Briefly, 100 mL of 0.01 wt% $HAuCl_4$ solution was heated to slight boiling in a flask, and then 4.0 mL of 1% trisodium citrate was added with stirring. After 30 min, the wine red AuNPs solution was obtained and cooled to room temperature. Finally, 100 mL AuNPs solution was centrifuged at 10000 rpm for 25 min and dispersed into 10 mL ultrapure water for further use.

2.3. Preparation the AuNFs modified ITO electrode

Before the preparation, the ITO coated glass electrodes were ultrasonically washed sequentially with acetone, 1:1 (v/v) NaOH (1 M)/ethanol mixture and ultrapure water (15 min each). The pretreated ITO was immersed in solution containing H_2O_2/NH_4OH (30%)/H_2O in the ratio of 1:1:5 for 90 min for creating a hydrophilic surface with hydroxyl groups. After washing thoroughly with ultrapure water and dried with a stream of N_2, the ITO electrode was immersed into 2% (v/v) APTES ethanol solution at room temperature overnight. Then, this obtained ITO slice was rinsed with ethanol and dried with N_2 gas, followed by curing at 100 °C for 30 min and cooled to room temperature. Subsequently, 35 μL of prepared AuNFs solution was coated on the surface of the APTES-modified ITO electrode and left undisturbed for 4 h at 4 °C to deposit the AuNFs. Finally, the AuNFs/ITO electrode was rinsed with ultrapure water and dried with N_2 gas. The same method was used for the preparation of the AuNPs modified ITO electrode.

2.4. Fabrication of the ECL immunosensor

Firstly, 25 μL of anti-AFP (20 μg mL^{-1}) PBS solution (0.1M pH 7.4) was dropped onto the AuNFs/ITO electrode surface, incubated for 1 h at 37 °C. After the electrode was rinsed with 0.1 M PBS (pH 7.4) to remove the residual anti-AFP, the anti-AFP/AuNFs/ITO electrode was blocked with 20 μL BSA solution (0.1%) incubated for 40 min to avoid non-specific binding. Then, the obtained electrode was washed with 0.1 M PBS (pH 7.4) to remove physically adsorbed BSA. As a result, we obtained the final sensor and filled it with PBS (pH 7.4) and stored at 4 °C.

2.5. Analysis procedure

The final sensor electrode was immersed in 0.1 M PBS (pH 7.4) spiked with various concentrations of AFP at 37 °C for 20 min. Afterward, it was washed with 0.1 M PBS (pH 7.4) carefully. Finally, the sensor electrode was transferred to 0.2 mM luminol containing 0.1 M Tris (pH 9.5) and put in the ECL cell. After soaking for 20 min, ECL signal was recorded for the quantitative analysis of AFP. The photomultiplier tube (PMT) was set at 750 V and working potential was 0–1.0 V. The scan rate was set at 100 mV/s.

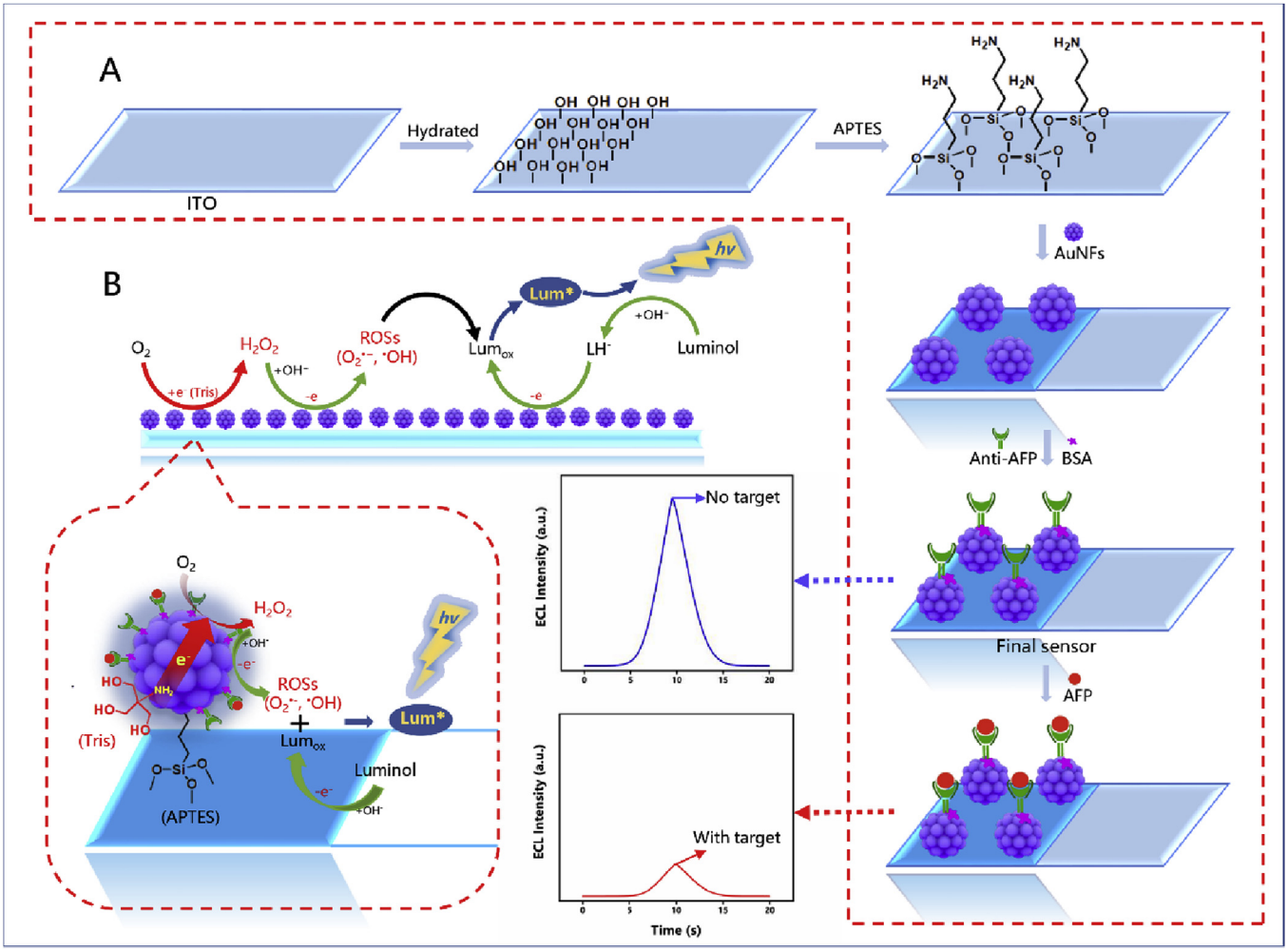

Scheme 1. Schematic illustration of (A) fabrication process of BSA/anti-AFP/AuNFs/ITO immunosensor; (B) possible ECL mechanism of the luminol-O_2 system.

3. Results and discussion

3.1. Structural and optical properties of AuNFs

In this study, the growth of gold seeds is used to prepare AuNFs. The SEM image shows that multitipped AuNFs were well-dispersed nanoparticles and the statistical particle size distribution of the AuNFs (Fig. 1A, inset) was mainly in the range of 45–84 nm with an average diameter of 65.1 nm, and each AuNF outer layer has a plurality of spherical subunits (bright dots) (Fig. 1A). Furthermore, from the inserted high-resolution SEM (HRSEM) photo, it can be observed that the surface of the AuNF is covered with irregularly shaped gold nanoparticles which form some edges, corners and tip regions. These regions may provide abundant active sites that act as tiny conduction centers to promote electron transport and enhance catalytic activity of AuNFs. High-resolution TEM (HR-TEM) measurements of the AuNFs showed that many well-resolved lattice fringes (Fig. 1B). Meanwhile, the (100) and (111) sub-surfaces of the AuNFs edges and corners form low-coordinate atomic steps, and these small facets are combined to further form the (211) high-index facets that match the corresponding atomic model (Fig. 1C), which provide sufficient active sites available for reactants (Fujita et al., 2012; Maity et al., 2014; Ye et al., 2016). The crystal structures of AuNFs were also studied by XRD techniques. The XRD pattern displays five Au diffraction peaks at $2\theta = 38.12$, 44.27, 64.42, 77.85, and 81.49° which are assigned to (111), (200), (220), (311), and (222) planes of the face-centered-cubic (fcc) gold. As shown in Fig. 1E, the monodisperse AuNPs were 15 ± 2 nm in diameter. Fig. 1F showed the normalized UV–vis spectra of the prepared AuNFs and AuNPs, and the absorption peak of AuNFs was observed to be significantly red-shifted due to the increase in particle size.

3.2. Electrochemical investigation of the assembly steps of the ECL biosensor

CV and EIS techniques were considered as optimal tools for characterizing step-by-step assembly of immunosensors, which can show changes of ITO electrode behavior after each modification step. As shown in Fig. 2A, a pair of symmetric redox peaks (curve a) were acquired which corresponded to the reversible redox reaction of $[Fe(CN)_6]^{3-/4-}$ on the bare ITO. The oxidation and reduction peak currents increased after APTES modification due to the protonation of positively charge amino group in aqueous solution (Khan et al., 2018) (curve b). When AuNFs were cast onto the APTES/ITO electrode, the peak current clearly improved duo to AuNFs could supply a larger surface area and facilitate surface electron transfer. (curve c). By further attaching anti-AFP and bovine serum albumin (BSA) (curve d), the redox peak current significantly decreased due to the electron inertness of anti-AFP and BSA. Obviously, the decreased peak current was observed after AFP combined with the BSA/anti-AFP/AuNFs/ITO electrode (curve e).

The electron-transfer resistance (R_{et}) is an important indicator reflecting the impedance changes of the electrode surface, can be explained by semicircle diameter from EIS measurements. As shown in Fig. 2B, compared with the bare ITO electrode (curve a), the R_{et} significantly decreased after APTES (curve b) and AuNFs (curve c) were covered on ITO electrode due to easy electronic transport at the

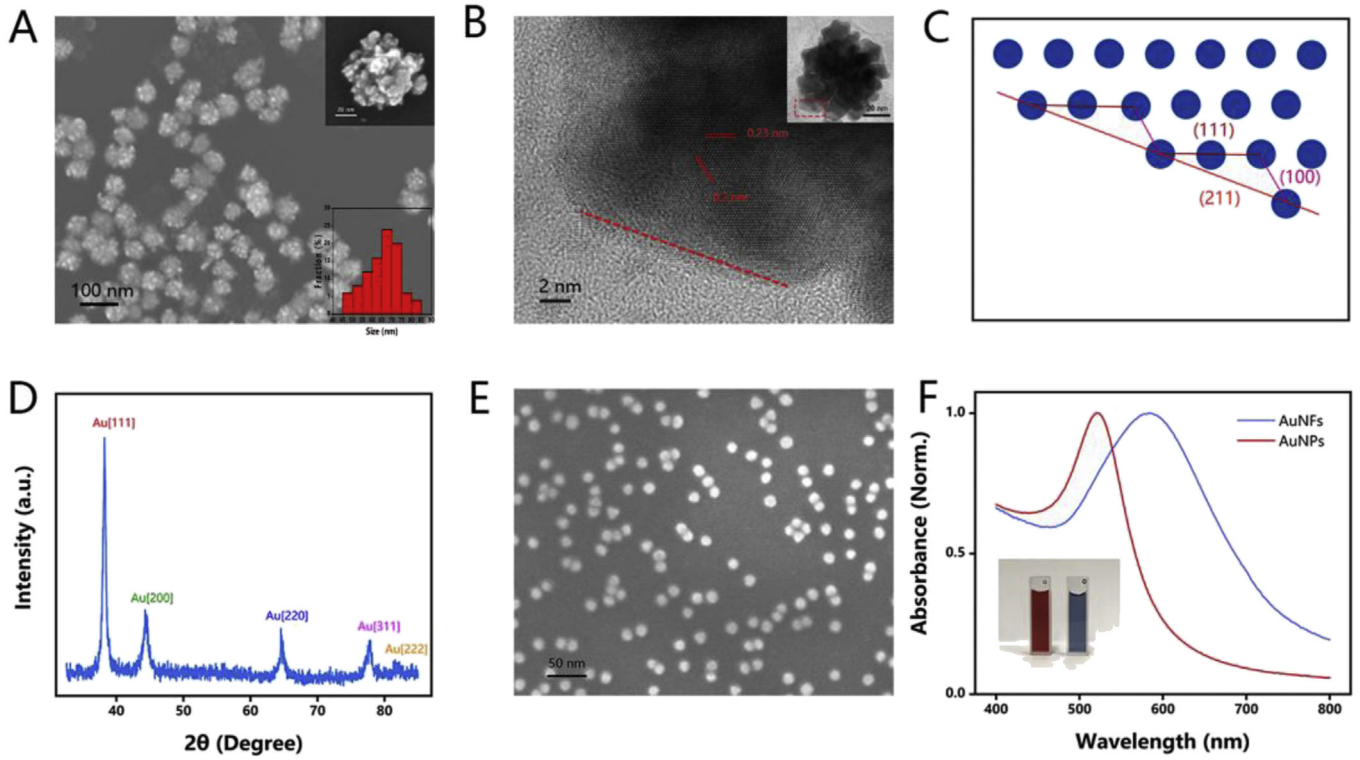

Fig. 1. (A) SEM image of AuNFs. Inset: HRSEM image and size distribution of AuNFs.; (B) HR-TEM image of the AuNF. Inset: TEM images of a single AuNF; (C) The corresponding atomic models of {211} planes; (D) Wide-angle XRD profile of AuNFs. (E) SEM image of AuNPs; (F) Normalized UV–vis spectrum of AuNFs and AuNPs. Inset: solution of AuNPs (left) and AuNFs(right).

electrode solution interface. However, the R_{et} values continuously increased after the anti-AFP and BSA (curve d) loading onto the AuNFs surface, indicating that the immobilized anti-AFP and BSA impeded electron exchange on the electrode surface. When AFP was combined on the final sensor, the R_{et} value becomes larger (curve e) due to the formation of immune complexes, which further blocked electron conduction on the electrode surface. The EIS spectra showed an electron transfer trend similar to the CV curves, proving that the successful assembly of the immunosensor.

3.3. Possible mechanism of catalyzing the generation of H_2O_2 by AuNFs as the coreactant accelerator

The possible mechanism of catalyzing the generation of H_2O_2 was studied by taking UV–vis absorption spectra, Raman spectra and ECL measurements.

As shown in Fig. 3A, several known concentrations of H_2O_2 in 1 M Tris have an absorption peak around 214 nm (curve a, b, c) because under alkaline conditions, the hydroperoxyl ion formed after deprotonation of H_2O_2 has a broad absorption band in the vicinity (Higashi et al., 2018; Song et al., 2017). At the same time, we soaked the AuNFs/ITO or AuNPs/ITO electrode (prepared at the same concentration of

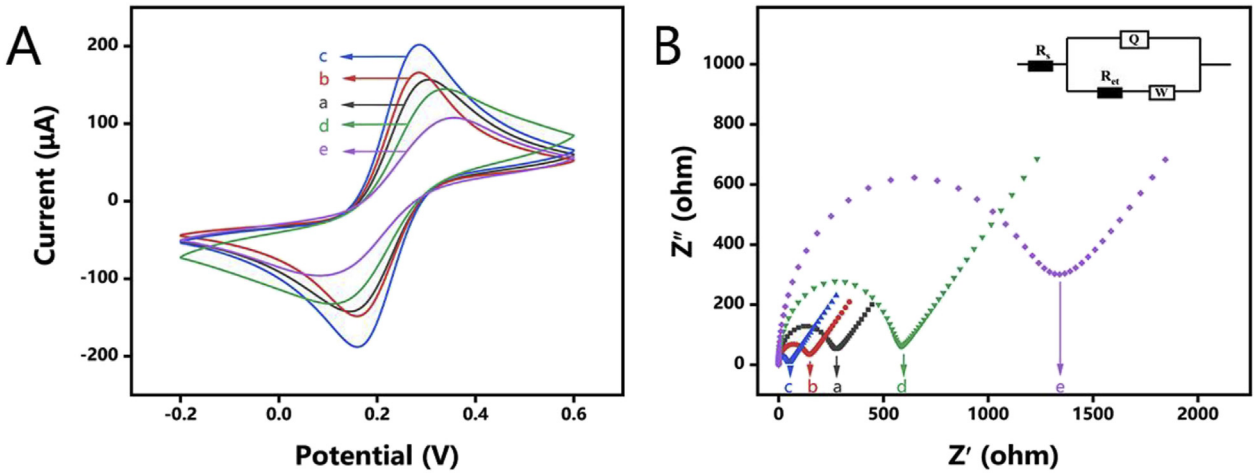

Fig. 2. (A) CV curves and (B) EIS spectra of (a) ITO, (b) APTES/ITO, (c) AuNFs/APTES/ITO, (d) final sensor and (e) AFP/BSA/anti-AFP/AuNFs/APTES/ITO in 0.1 M KCl containing 5 mM $[Fe(CN)_6]^{3-/4-}$. The inset of (B) shows the equivalent circuit. The scan rate of CV is 50 mV/s. The frequency range is from 0.1 to 100 kHz with amplitude of 5 mV.

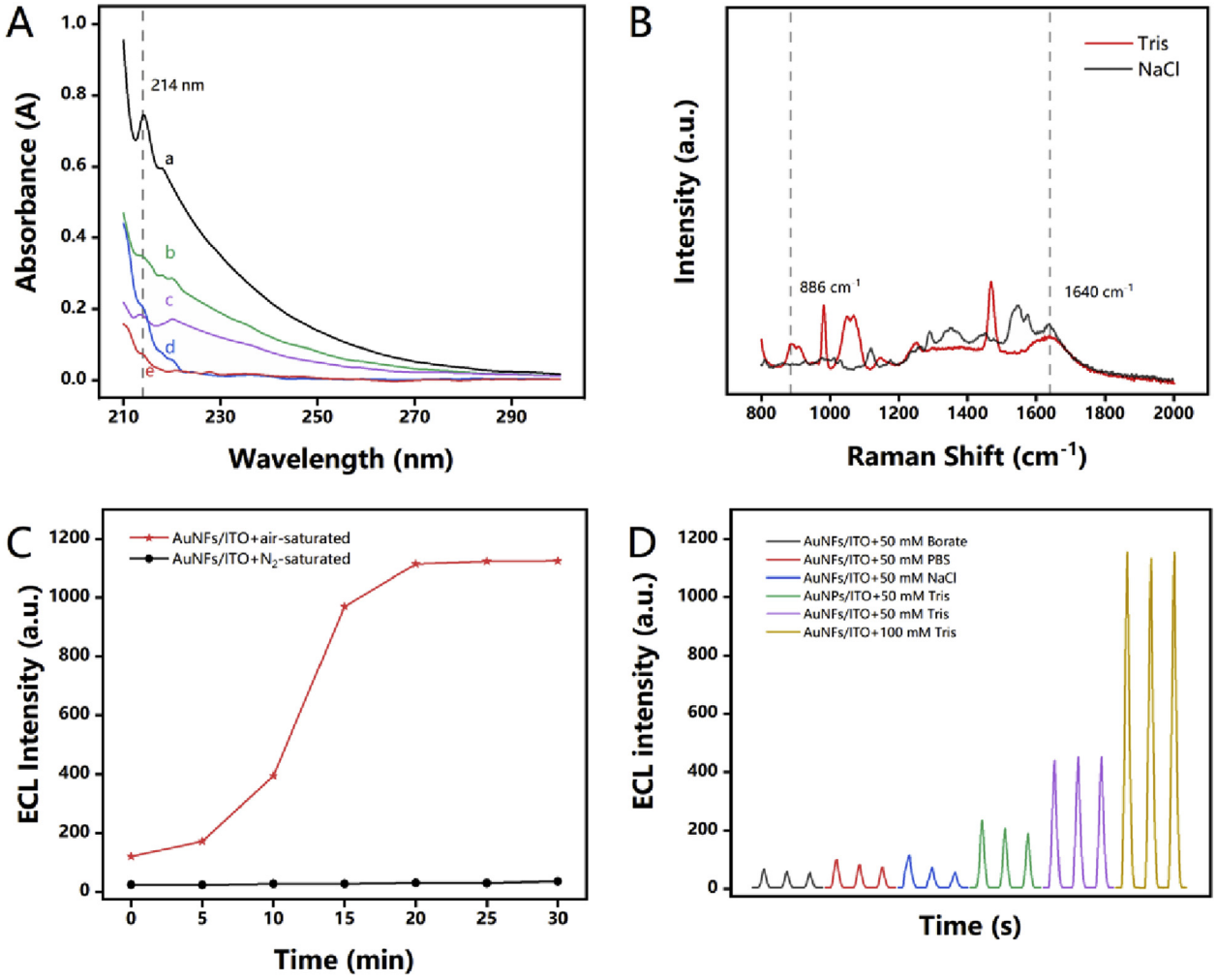

Fig. 3. (A) UV–vis spectrum of (a) 0.4 mM H_2O_2, (b) 0.2 mM H_2O_2, (c) 0.1 mM H_2O_2 (all contain 1 M Tris), and Tris solution after soaked for 10 min by (d) AuNFs/ITO electrode, (e) AuNPs/ITO electrode; (B) Raman spectra of AuNFs/ITO electrode surface dripped with Tris and NaCl solution; (C) ECL intensity of AuNFs/ITO electrode in Tris solution (pH 8.0) with and without continuous N_2 sparging; (D) ECL intensity of AuNFs/ITO or AuNPs/ITO electrode in various solutions after 20 min (contain 0.2 mM luminol; pH 8.0; scan potential from 0 to 0.8 V).

AuNFs and AuNPs) in 5 mL 1 M Tris solution under the same conditions for 10 min. By comparing the UV–vis absorption spectra, we found that the absorption peak of the Tris solution soaked by the AuNFs/ITO electrode (curve d) near 214 nm was significantly higher than the Tris solution soaked by the AuNPs/ITO electrode (curve e). These results indicate that multitipped AuNFs catalyze the production of H_2O_2, and its catalytic activity is much higher than that of AuNPs.

To further investigate the possible path of H_2O_2 generation, we dripped 30 μL of 1 M Tris or NaCl solution onto the AuNFs/ITO electrode. After 10 min, the Raman spectra of the electrode surface were measured and compared (without drying the sample) (Fig. 3B). Comparing the Raman spectra in these two cases, we found that the peak intensity of the electrode dropped by Tris at 1640 cm^{-1} corresponding to O_2 vibrational mode (Kong et al., 2012) was significantly decreased. At the same time, the electrode dropped by Tris also showed a strong peak at 886 cm^{-1}, which is the vibrational mode of H_2O_2 (He et al., 2019; Li and Gewirth, 2003). However, we did not observe this peak on the electrode dropped by NaCl solution. The decrease in O_2 content and the increase in H_2O_2 content indicate that under the electron donating effect of Tris, O_2 adsorbed on the surface of AuNFs can be catalyzed by some form of electron transfer to produce H_2O_2.

To verify the above process, the effect of dissolved O_2 on the production of H_2O_2 was investigated by AuNFs/ITO electrode immersed in Tris (containing 0.2 mM luminol) with or without continuous N_2 gas sparging (Fig. 3C). In the N_2-saturated solution where dissolved O_2 was removed, the AuNFs/ITO electrode showed no significant luminescence. However, the ECL signal of the AuNFs/ITO electrode increased with increasing soaking time in air-saturated Tris solution and reached a maximum at 20 min. This result indicates that dissolved O_2 as the coreactant can be adsorbed on the surface AuNFs to catalyze the production of H_2O_2 and accelerate the ECL reaction in Tris solution.

Furthermore, we explored the ECL performance of the AuNFs/ITO and AuNPs/ITO electrodes in various solutions. Fig. 3D shows that the AuNFs/ITO electrode in the borate buffer, PBS buffer and NaCl solution or AuNPs/ITO electrode in Tris solution, the related ECL signals presented poor stability as a result of inefficient ECL reactions and the changed microenvironment of the system. However, a significant ECL signal was observed after the AuNFs/ITO electrode was immersed in Tris solution and amplified with the increased concentration of Tris. This may be ascribed to multitipped AuNFs with abundant active sites catalyzing the production of H_2O_2 using the electron donating effect of Tris, followed by continuous supply of electrogenerated ROSs to greatly stabilize and enhance the intensity of the ECL signal.

Based on these experimental results, we propose a hypothetical mechanism for AuNFs to catalyze the production of H_2O_2. First, dissolved O_2 is adsorbed on the surface of AuNFs. Then, the amino and hydroxyl groups of the Tris are oxidized by AuNFs, followed by electrons transfer to the adsorbed O_2 and activation of the O_2 utilizing the

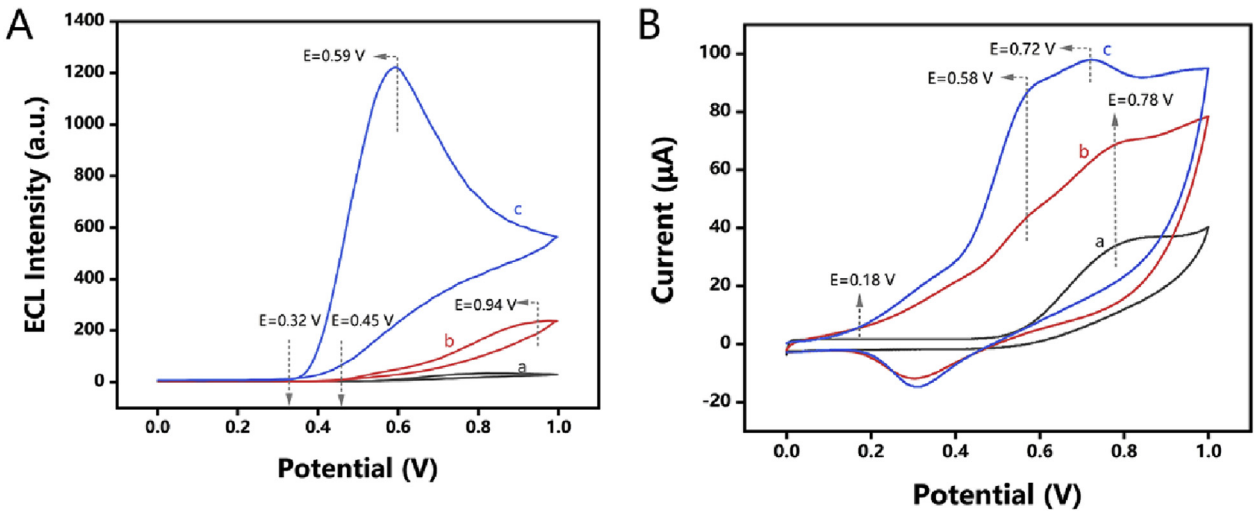

Fig. 4. (A) ECL intensity and (B) CV curves of (a) AuNFs/ITO electrode in N_2-saturated, (b) AuNPs/ITO electrode in air-saturated, and (c) AuNFs/ITO electrode in air-saturated solution (both contain 0.2 mM luminol and 0.1 M Tris, pH 8.0; scan rate 100 mV/s).

active sites on the surface of the multitipped AuNFs. Finally, the activated O_2 is reduced to form and release H_2O_2 by means of an oxidase-type enzyme.

3.4. Possible ECL mechanism of Luminol-O_2 system

In the presence of H_2O_2, H_2O_2 further produces various ROSs, which directly participate in the luminol ECL reaction of and significantly amplify the ECL signal (Kitte et al., 2017). To explore this process and related mechanisms, we compared the ECL and CV responses of AuNF/ITO and AuNPs/ITO electrodes immersed in different luminol solutions. As shown in Fig. 4A, an almost invisible ECL signal was obtained with AuNFs/ITO electrode in N2-saturated solution (curve a), revealing that AuNFs does not directly enhance luminol ECL intensity without O_2. When the AuNPs/ITO electrode was immersed in air-saturated solution, the ECL intensity was only increased to 240 a. u. at 0.94 V (curve b), indicating that AuNPs has limited enhancement of luminol ECL signal in the presence of O_2. However, when the AuNFs/ITO electrode was introduced into the air-saturated solution (curve c), the ECL signal increased significantly from 240 a. u. to 1227 a. u. (about 5-fold amplification). At the same time, the initial potential of the corresponding peak was negatively shifted from 0.45 to 0.32 V and reached a maximum at 0.59 V. These results further indicate that the coreaction accelerator AuNFs did improve the efficiency of the ECL reaction of dissolved O_2 and luminol.

Accordingly, the CV curves were shown in Fig. 4B. When the AuNFs/ITO electrode was immersed in N_2-saturated solution, the electrode has only one oxidation peak at 0.78 V with a low current value (curve a). This phenomenon further indicates that AuNFs are not directly involved in the oxidation reaction of luminol. When the AuNPs/ITO electrode was immersed in air-saturated solution, a pair of redox peaks appeared with two weak oxidation peaks at 0.58 V and 0.78 V (curve b). These two oxidation peaks may be related to the production of luminol radicals and diazaquinone, respectively (Nagatani et al., 2016). Despite the presence of O_2 in the system, the low catalytic activity of AuNPs resulted in low oxidation efficiency and weak ECL signal for luminol. However, after the AuNFs/ITO electrode was immersed in air-saturated solution, the charging current of the luminol was significant increased from 0.18 V and the strong anodic peak shifted negatively from 0.78 to 0.72 V (curve c). This may be due to the sufficient H_2O_2 involvement in the oxidation reaction of luminol and reduction of the overpotential from the interaction between luminol and various ROSs produced by H_2O_2 (Kitte et al., 2017). These results revealed that under the electron donating effect of Tris, AuNFs as the coreactant accelerator does catalyze the production of H_2O_2 from dissolved O_2 and further produces sufficient ROSs at anode potential to accelerate the ECL reaction of luminol.

Combining the reference (Kitte et al., 2017; Nagatani et al., 2016; Wu et al., 2018) with our experimental results, the possible luminescence mechanisms of luminol-O_2 ECL systems were shown in Scheme. 1B. In conclusion, the dissolved O_2 was first catalyzed on the surface of AuNFs to produce H_2O_2 using Tris as an electron donor. Then, Luminol was oxidized to oxidation of luminol (Lum_{ox}) upon anodic potential scanning at AuNFs/ITO electrode. Finally, oxidation of luminol reacts with electrogenerated ROSs from H_2O_2 to generate the excited-state 3-aminophthalate anion (Lum*), which produced a significant ECL emission.

3.5. Analytical performance of the resulting sensor

The resulting immunosensor with a higher ECL intensity will have a wider detection range. Therefore, we optimized the time of AuNFs decoration and the pH of the Tris buffer to improve the ECL signal intensity (Figs. S1A and C). At the same time, in order to obtain the resulting immunosensor with higher performance, we optimized the incubation time of anti-AFP and AFP (Figs. S1B and D).

These ECL signals are collected when different concentrations of AFP standards specifically combined with antibodies on the resulting sensor. As shown in Fig. 5A, because the combination of AFP and anti-AFP inhibits the electron transfer, which decelerate the rate of ECL reaction, the ECL intensities decrease with increasing of the AFP concentration from 0.01 to 100 ng mL^{-1} and presented an excellent linear relationship with the logarithm of AFP concentration (Fig. 5B). The corresponding calibration curve is described as ECL = $-754.73\ \lg C_{AFP} + 2142.3$ ($R^2 = 0.991$), with a detection limit of 3.4 pg mL^{-1} (S/N = 3). In addition, Table S1 shows the linear range and detection limit of previously reported immunosensors. Compared to other reports, the prepared immunosensor showed a large linear range and a low detection limit.

Some very important features of this immunosensor, including selectivity and stability need to be validated. According to Fig. 5C, the developed immunosensors with some other potential interferents showed almost the same response as the blank solution, indicating that the obtained immunosensor has high selectivity and specificity for the detection of AFP.

Finally, we studied the stability of the AFP immunosensor. The final sensor was stored in PBS buffer (pH 7.4) at 4 °C throughout the test period. The ECL intensity of the stored sensor retained about 91% of its

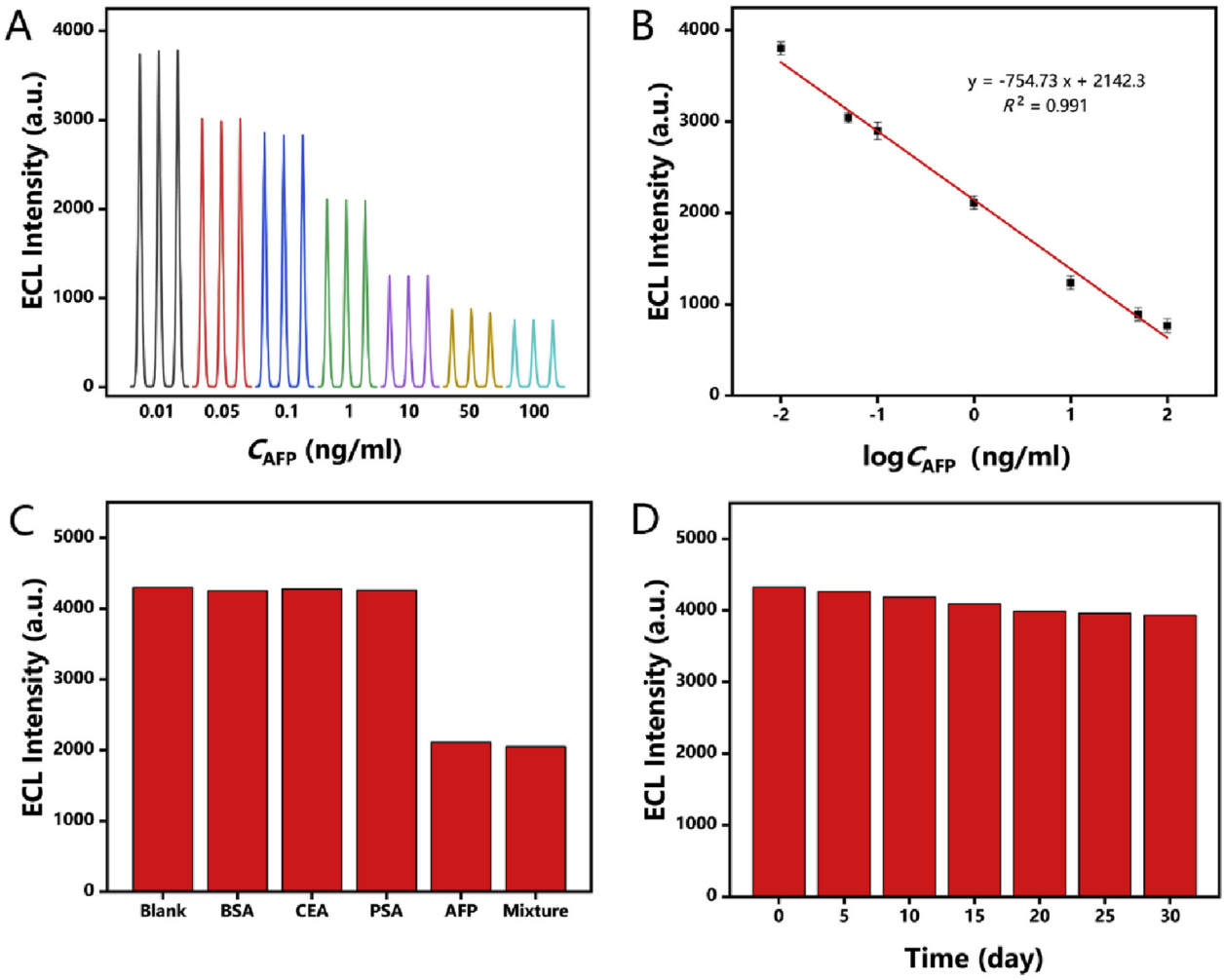

Fig. 5. (A) ECL responses with different concentration of AFP; (B) calibration curve for AFP determination; (C) specificity of the AFP immunosensor; (D) stability of the stored sensor over a 30 day period.

initial value after 1 month (Fig. 5D), indicating that the sensor exhibits high stability.

3.6. Preliminary analysis of real samples

In order to investigate the feasibility of the AFP immunosensor for clinical determination, some human serum samples were measured by the standard addition method. Different concentrations of AFP were added to human serum and measured by using the prepared immunosensor. According to Table S2, these data showed that the recovery (between 95.4% and 113.0%) were acceptable, and the relative standard deviation (RSD) was less than 3.97%, which indicated that the designed immunosensor had potential applicability for reliable detection of AFP in clinical analyses.

4. Conclusions

In conclusion, an enzyme-free and label-free ECL immunosensor for the detection of AFP has been demonstrated combining dissolved O_2 as the endogenous coreactant and AuNFs as a coreaction accelerator in the luminol-dissolved O_2 ECL system. Benefiting from its unique morphological characteristics, AuNFs exhibited a strong catalytic activity to reduce O_2 to H_2O_2 and significantly increase the ECL signal intensity. Meanwhile, the ECL mechanism of luminol-dissolved O_2 system was initially studied. The resulting sensor exhibited good analytical characteristics, excellent selectivity, long-term stability, and reproducibility in AFP analysis. In addition, the proposed ECL immunosensor was successfully applied to the detection of AFP in spiked human serum samples. Moreover, the strategy is low in cost and easy to operate, and in the future, combined with portable inspection device will make it more suitable for clinical use as a disposable device in POCTs. We believe that this research provides a reliable approach and a great opportunity for further development of luminol-based ECL system.

CRediT authorship contribution statement

Qiuyu Hu: Conceptualization, Data curation, Formal analysis, Methodology, Visualization, Writing - original draft. **Jianying Yang:** Investigation, Resources, Supervision, Validation. **Zengyao Zheng:** Investigation, Resources, Supervision, Validation. **Yupei Ding:** Data curation, Formal analysis, Resources. **Yaowen Chen:** Formal analysis, Resources, Software. **Wenhua Gao:** Funding acquisition, Project administration, Resources,Supervision, Validation, Writing - review & editing.

Declaration of competing interest

The authors declare that they have no known competing financial interests or personal relationships that could have appeared to influence the work reported in this paper.

Acknowledgements

We are grateful for the financial support from the Natural Science Foundation of Guangdong Province (No. 2014A030313480) and the Science & Technology Project of Guangdong Province (No. 2016A020223014).

Appendix A. Supplementary data

Supplementary data to this article can be found online at https://doi.org/10.1016/j.bios.2019.111627.

References

Alonso-González, P., Albella, P., Schnell, M., Chen, J., Huth, F., García-Etxarri, A., Casanova, F., Golmar, F., Arzubiaga, L., Hueso, L.E., Aizpurua, J., Hillenbrand, R., 2012. Nat. Commun. 3.
Bera, K., Ghosh, T., Basak, S., 2015. J. Phys. Chem. C 119, 1800–1808.
Chirumamilla, M., Toma, A., Gopalakrishnan, A., Das, G., Zaccaria, R.P., Krahne, R., Rondanina, E., Leoncini, M., Liberale, C., De Angelis, F., Di Fabrizio, E., 2014. Adv. Mater. 26, 2353–2358.
Cui, Q., He, F., Wang, X., Xia, B., Li, L., 2012. ACS Appl. Mater. Interfaces 5, 213–219.
Daniel, M.-C., Astruc, D., 2004. Chem. Rev. 104, 293–346.
Das, P., Chini, T.K., 2012. J. Phys. Chem. C 116, 25969–25976.
Das, P., Chini, T.K., Pond, J., 2012. J. Phys. Chem. C 116, 15610–15619.
Dong, Y.-P., Cui, H., Xu, Y., 2007. Langmuir 23, 523–529.
Fang, Q., Lin, Z., Lu, F., Chen, Y., Huang, X., Gao, W., 2019. Electrochim. Acta 302, 207–215.
Farka, Z., Juřík, T., Kovář, D., Trnková, L., Skládal, P., 2017. Chem. Rev. 117, 9973–10042.
Fujita, T., Guan, P., McKenna, K., Lang, X., Hirata, A., Zhang, L., Tokunaga, T., Arai, S., Yamamoto, Y., Tanaka, N., 2012. Nat. Mater. 11, 775.
Gao, H., Wen, L., Wu, Y., Yan, X., Li, J., Li, X., Fu, Z., Wu, G., 2018. J. Agric. Food Chem. 66, 5247–5253.
Hao, F., Nehl, C.L., Hafner, J.H., Nordlander, P., 2007. Nano Lett. 7, 729–732.
He, Y., Yang, X., Yuan, R., Chai, Y., 2019. J. Mat. Chem. B 7, 2643–2647.
Higashi, Y., Mazumder, J., Yoshikawa, H., Saito, M., Tamiya, E., 2018. Anal. Chem. 90, 5773–5780.
Hrelescu, C., Sau, T.K., Rogach, A.L., Jäckel, F., Laurent, G., Douillard, L., Charra, F., 2011. Nano Lett. 11, 402–407.
Huang, X., Deng, X., Qi, W., Wu, D., 2018. Sens. Actuators B Chem. 273, 466–472.
Khan, M.Z.H., Liu, X., Zhu, J., Ma, F., Hu, W., Liu, X., 2018. Biosens. Bioelectron. 108, 76–81.
Kitte, S.A., Gao, W., Zholudov, Y.T., Qi, L., Nsabimana, A., Liu, Z., Xu, G., 2017. Anal. Chem. 89, 9864–9869.
Kong, X., Sun, Z., Chen, Q., 2012. Phys. Chem. Chem. Phys. 14, 13564.
Li, M.-X., Feng, Q.-M., Zhou, Z., Zhao, W., Xu, J.-J., Chen, H.-Y., 2017. Anal. Chem. 90, 1340–1347.
Li, X., Gewirth, A.A., 2003. J. Am. Chem. Soc. 125, 7086–7099.
Li, S.-F., Zhang, X.-M., Du, W.-X., Ni, Y.-H., Wei, X.-W., 2008. J. Phys. Chem. C 113, 1046–1051.
Liu, X., Fang, C., Yan, J., Li, H., Tu, Y., 2018. Bioelectrochemistry 123, 211–218.
Liu, Z., Qi, W., Xu, G., 2015. Chem. Soc. Rev. 44, 3117–3142.
Maity, A., Maiti, A., Das, P., Senapati, D., Kumar Chini, T., 2014. ACS Photonics 1, 1290–1297.
Mo, G., He, X., Zhou, C., Ya, D., Feng, J., Yu, C., Deng, B., 2019. Biosens. Bioelectron. 126, 558–564.
Myroshnychenko, V., Nelayah, J., Adamo, G., Geuquet, N., Rodríguez-Fernández, J., Pastoriza-Santos, I., MacDonald, K.F., Henrard, L., Liz-Marzán, L.M., Zheludev, N.I., Kociak, M., García de Abajo, F.J., 2012. Nano Lett. 12, 4172–4180.
Nagatani, N., Inoue, Y., Araki, A., Ushijima, H., Hattori, G., Sakurai, Y., Ogidou, Y., Saito, M., Tamiya, E., 2016. Electrochim. Acta 222, 580–586.
Peng, Z., Chen, Z., Jiang, J., Zhang, X., Shen, G., Yu, R., 2007. Anal. Chim. Acta 583, 40–44.
Qiao, Y., Li, Y., Fu, W., Guo, Z., Zheng, X., 2018. Anal. Chem. 90, 9629–9636.
Song, M., Wang, J., Chen, B., Wang, L., 2017. Anal. Chem. 89, 11537–11544.
Song, S., Qin, Y., He, Y., Huang, Q., Fan, C., Chen, H.-Y., 2010. Chem. Soc. Rev. 39, 4234.
Tsunoyama, H., Ichikuni, N., Sakurai, H., Tsukuda, T., 2009. J. Am. Chem. Soc. 131, 7086–7093.
Wang, T., Song, X., Lin, H., Hao, T., Hu, Y., Wang, S., Su, X., Guo, Z., 2019. Anal. Chim. Acta 1062, 124–130.
Wu, F.F., Zhou, Y., Zhang, H., Yuan, R., Chai, Y.Q., 2018. Anal. Chem. 90, 2263–2270.
Xu, P., Li, J., Huang, X., Duan, H., Ji, Y., Xiong, Y., 2016a. Anal. Methods 8, 3316–3324.
Xu, S., Li, X., Li, C., Li, J., Zhang, X., Wu, P., Hou, X., 2016b. Anal. Chem. 88, 6418–6424.
Ye, S., Benz, F., Wheeler, M.C., Oram, J., Baumberg, J.J., Cespedes, O., Christenson, H.K., Coletta, P.L., Jeuken, L.J.C., Markham, A.F., Critchley, K., Evans, S.D., 2016. Nanoscale 8, 14932–14942.
Zhang, A., Xiang, H., Zhang, X., Guo, W., Yuan, E., Huang, C., Jia, N., 2016. Biosens. Bioelectron. 75, 206–212.
Zhuo, Y., Wang, H.-J., Lei, Y.-M., Zhang, P., Liu, J.-L., Chai, Y.-Q., Yuan, R., 2018. Analyst 143, 3230–3248.